Composition- and Condition-Dependent Kinetics of Homogeneous Ester Hydrogenation by a Mn-Based Catalyst

Krieger, Annika M.; Kuliaev, Pavel; Armstrong Hall, Felix Q.; Sun, Dapeng; Pidko, Evgeny A.

DOI
10.1021/acs.jpcc.0c09953

Publication date
2020

Document Version
Final published version

Published in
Journal of Physical Chemistry C

THE JOURNAL OF PHYSICAL CHEMISTRY C

pubs.acs.org/JPCC

Article

Composition- and Condition-Dependent Kinetics of Homogeneous Ester Hydrogenation by a Mn-Based Catalyst

Annika M. Krieger, Pavel Kuliaev, Felix Q. Armstrong Hall, Dapeng Sun, and Evgeny A. Pidko*

Cite This: J. Phys. Chem. C 2020, 124, 26990−26998

Read Online

ACCESS | Metrics & More | Article Recommendations | Supporting Information

ABSTRACT: The reaction medium and conditions are the key parameters defining the efficiency and performance of a homogeneous catalyst. In the state-of-the-art molecular descriptions of catalytic systems by density functional theory (DFT) calculations, the reaction medium is commonly reduced to an infinitely diluted ideal solution model. In this work, we carry out a detailed operando computational modeling analysis of the condition dependencies and nonideal solution effects on the mechanism and kinetics of a model ester hydrogenation reaction by a homogeneous Mn(I)-P,N catalyst. By combining DFT calculations, COSMO-RS solvent model, and the microkinetic modeling approach, the kinetic behavior of the multicomponent homogeneous catalyst system under realistic reaction conditions was investigated in detail. The effects of the reaction medium and its dynamic evolution in the course of the reaction were analyzed by comparing the results obtained for the model methyl acetate hydrogenation reaction in a THF solution and under solvent-free neat reaction conditions. The dynamic representations of the reaction medium give rise to strongly nonlinear effects in the kinetic models. The nonideal representation of the reaction medium results in pronounced condition dependencies of the computed energetics of the elementary reaction steps and the computed kinetic profiles but affects only slightly such experimentally accessible kinetic descriptors as the apparent activation energy and the degree of rate control.

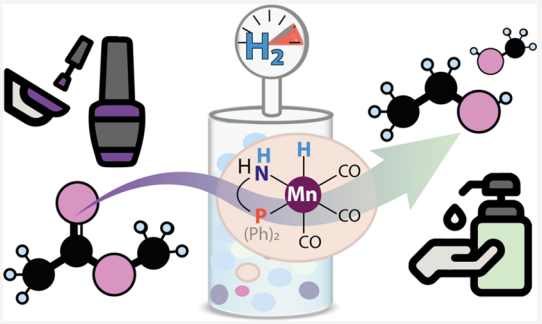

1. INTRODUCTION

Homogeneous catalysis by transition metal complexes is an important strategy for the efficient and sustainable production of chemical products and intermediates used in pharmaceuticals, fragrances, and fine chemicals.[1] Catalytic hydrogenation of unsaturated organic molecules with H_2 provides a highly atom-efficient and green alternative to the conventional stoichiometric synthetic routes utilizing inorganic hydrides as the reducing agents.[2] The development of new efficient hydrogenation catalyst systems based on earth-abundant, inexpensive, and biocompatible 3d metals is an important and active area of research.[3−7] Computations play an important role in modern catalysis and chemistry research by providing an atomistic framework to rationalize and support the experimental spectroscopic and reactivity studies[8,9] and increasingly in the recent years, to guide and support the experimental development and optimization of new and improved catalyst systems.[10−12]

Modern quantum chemistry, and in particular, density functional theory (DFT) methods provide practical and efficient computational tools to obtain detailed insights into the mechanisms of catalytic reactions, nature of key catalytic intermediates and transition states, and the associated energetics of the elementary steps.[13,14] The prediction of geometries and properties of reaction intermediates is usually accurate and consistent among different functionals.[15] DFT is very powerful, and efforts are continuously being made to develop more accurate computational methods based on new exchange−correlation functionals[16−18] and wave-function-based methods.[19]

When applied to practical problems of chemistry and catalysis, the computational accuracy is contributed by both the accuracy of the quantum chemical method and the accuracy/completeness of the chemical model used to represent the catalytic system in question.[20] The latter represents a particular challenge when simulating chemical processes in multicomponent concentrated reactive solutions commonly encountered in the practice of homogeneous catalysis. There is a substantial condition gap between the experiments with their highly complex multicomponent reaction systems and the highly reduced computational models. Operando modeling approaches are being developed to close this gap and enable the detailed in silico analysis of the condition dependencies in practical catalytic systems.

Received: November 4, 2020
Revised: November 10, 2020
Published: November 24, 2020

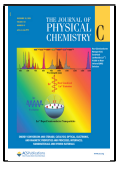

In applied computational catalysis, the reaction environment is commonly reduced to an oversimplified implicit ideal solvent model that does not account for all the solvation and complex medium effects.[21−23] Bridging the condition gap between the experiment and the model is an important challenge on the way toward predictive catalysis modeling.[24] Development of computational approaches to analyze the effect of the multicomponent reaction environment that includes solvent, reactants, as well as various promotors and additives is key to understanding the factors that define the catalytic performance. The choice of the reaction medium and conditions can determine whether the catalytic conversion takes place or not.[25,26] It is therefore important to investigate how the variations in the representation of the reaction environment and its composition affect the macro- and microscopic characteristics of a multicomponent catalytic reaction system.

Ester hydrogenation by homogeneous transition metal catalysts is an example of a highly complex multicomponent and multiphase catalyst system.[27−30] In the past, catalytic systems based on ruthenium, iron, osmium, and manganese have been investigated thoroughly.[31−40] However, a vast majority of studies have been devoted to ester hydrogenation by Ru- or Fe-based catalysts.[41−44] Following the first report by Beller and co-workers on a Mn-catalyst for the ester hydrogenation processes,[45] manganese has been in the focal area of homogeneous hydrogenation catalysis research in view of its abundance and biocompatibility.[46−49] For these systems, different mechanisms have been proposed and the presence of a solvent, additives, and base seems to be crucial for the catalytic reaction.[50,51] Because of the diversity in conditions and substrate scope, it remains challenging to analyze their specific contributions to the reactivity of the catalyst. This highlights the need to switch to a more complex system description and analysis. One widely employed method to analyze catalytic systems under the reaction conditions (operando) is microkinetic modeling.[24] However, its application to homogeneous catalysis is still relatively scarce.[52]

Our group has reported an ester hydrogenation catalytic system based on a nonpincer Mn-P,N catalyst, whose performance is defined by the multicomponent reaction environment (Figure 1).[47] Mechanistic studies combining

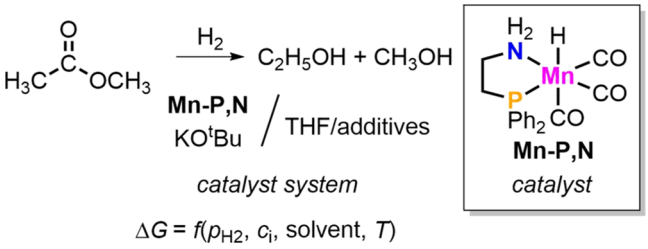

Figure 1. Definition of the condition space and the associated condition-dependent free energy surfaces for the catalytic ester hydrogenation reaction.

DFT calculations and ab initio thermodynamic analysis of multicomponent reactive solutions[25] highlighted the role of the complexity of the reaction environment in such systems and put forward a hypothesis on the mechanistic role of the base promotors and the concentrated reaction medium in this system.[50] The base additive plays a role in both catalyst activation and catalytic ester conversion itself.[53,54] Excess base helps removing trace amounts of water, aids substrate prearrangement, and supplements the entropic effects in base-assisted ester activation by Mn-P,N. Moreover, it has been proposed[50] that the inorganic base promotes hydrogenolysis paths to reactivate the alkoxide resting state.

Previously, the operando modeling of the multicomponent solution has been used to analyze condition dependencies of the thermodynamics of competing reaction paths to identify potential deactivating channels and resting states.[50] The properties of the reaction environment dynamically change in the course of the catalytic reaction from an ester (apolar, $\varepsilon(CH_3COOCH_3)_{298K} = 6.7$)[55] to alcohol (polar, $\varepsilon(CH_3OH)_{298K} = 33.6$, $\varepsilon(C_2H_5OH)_{298K} = 24.3$).[56,57] We anticipate that such an evolution of the medium and the associated condition dependencies will affect the reaction kinetics as well. Therefore, in this study, we examine the influence of different solvent descriptions on the computed reactivity of the Mn-P,N-based ester hydrogenation system.

This work reports the development of an operando DFT-based kinetic model accounting for the multicomponent and dynamic nature of the Mn-P,N homogeneous ester hydrogenation catalyst system. Four different approaches of varying complexity were considered to account for the solvation environment, as illustrated in Figure 2. The basic gas-phase

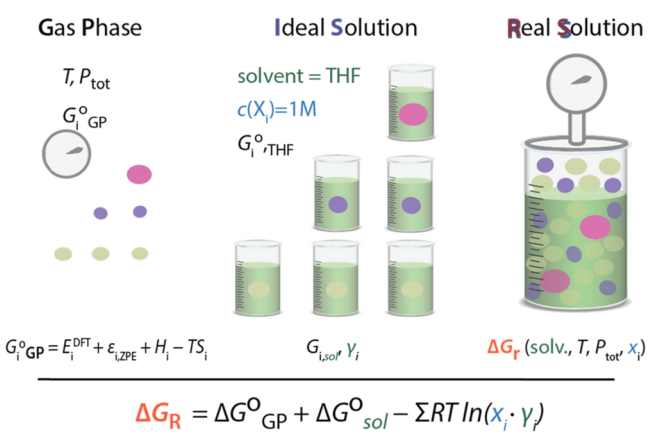

Figure 2. Models and approaches to concentration-dependent free energy surfaces.

model (***GP***) completely neglects the solvent environment.[58] The reaction components in this model are considered as separate noninteracting species, while the reaction conditions are accounted for here via the entropic and finite temperature corrections computed from statistical thermodynamics in the ideal gas approximation.[22] The ***IS*** model stands for ideal solution in which the bulk solvent effects are accounted for via the COSMO-RS implicit solvent model[59] but the components are considered as noninteracting. Here, a mixed-solvent model of THF and KOtBu base promotor was used to mimic the experimental conditions. However, in the experiments, the substrates and the products account for a substantial fraction of the reaction mixture. During the catalytic reaction, the ester substrate converts gradually to an alcohol product. Together with the reaction environment, dielectric constants, hydrogen bonding patterns, and the mode of solvation changes. To account for these effects, we introduced the concentration gradient corrections in the dynamic real solution (***RS***) models for the reaction in the THF solvent (***RS-THF***) and under solvent-free neat conditions (***RS-pure***). In the latter, the starting solvent is a reactant that is being fully converted to

https://dx.doi.org/10.1021/acs.jpcc.0c09953
J. Phys. Chem. C 2020, 124, 26990−26998

Scheme 1. Mechanisms of the Hydrogen Shuttle (HS) and Alkoxide (AX) Paths for a Model Methyl Acetate Ester Hydrogenation with Mn-P,N Catalyst I

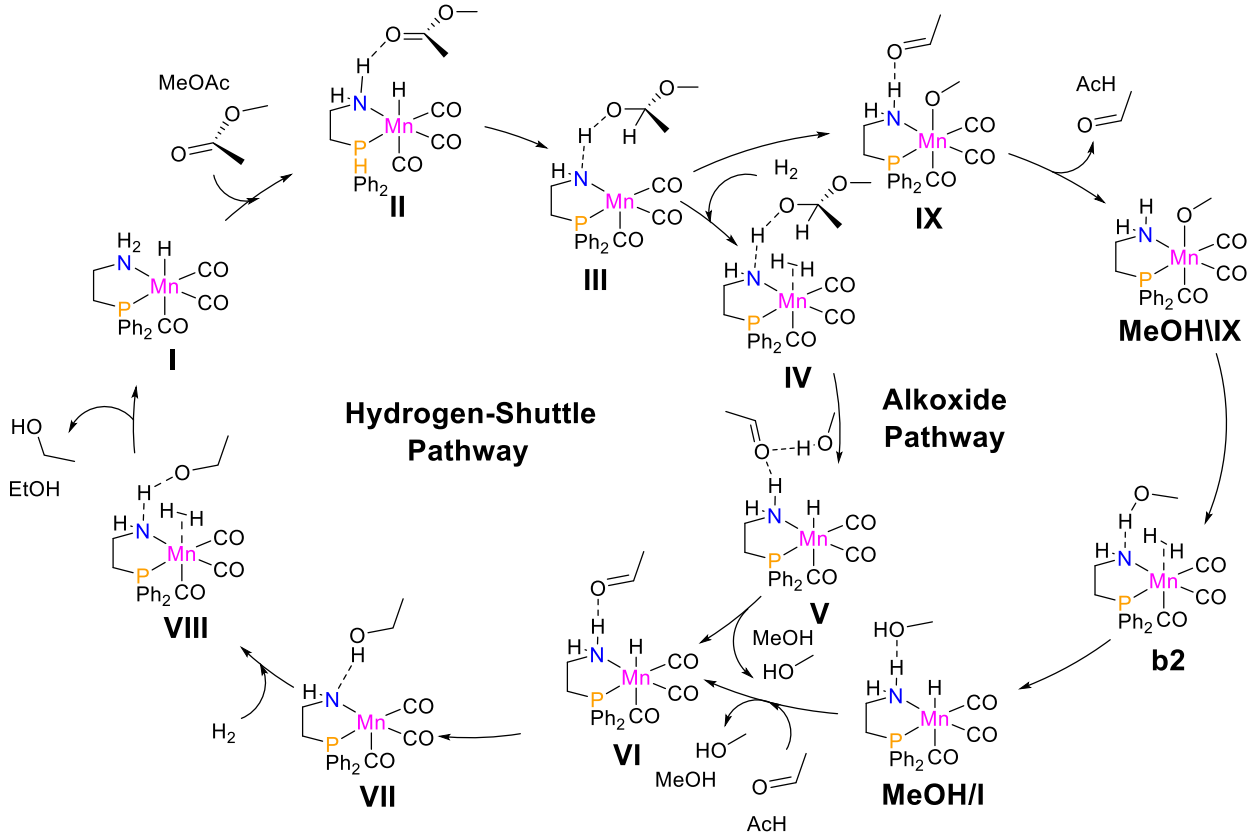

another solvent, that is, the product, therefore changing the properties of the solution completely. The ***RS-THF*** model resemble the common lab conditions. The mixed-solvent model is considered with realistic concentrations of the reagents and products as the reaction proceeds in THF as the main solvent.

The paper is organized into three sections. After describing the details of computational methodologies in Section 2, the results and discussion Section 3 begins with the introduction of the two competitive mechanisms and the presentation of the standard DFT results for the respective reaction paths. This is followed by the discussion of the effect of the solvent model on the computed free energy profiles, which are further utilized to construct a full condition-dependent microkinetic description of the system. The main findings and observations are summarized in the conclusion Section 4.

2. COMPUTATIONAL DETAILS

Geometry optimization and frequency analysis for intermediates and transition states were carried out in the framework of DFT using the Gaussian16 C0.1 program.[60] The hybrid exchange−correlation functional PBE0[61] was used in combination with the 6−311+G(d,p) basis set on all atoms for geometry optimization and vibrational analysis. Van der Waals interactions are accounted for by the DFT-D3 (BJ) method.[62] An ultrafine grid was uniformly used. The nature of each stationary point was confirmed by frequency analysis in which zero imaginary frequencies for minima and one for transition states were found. Reaction (ΔE) and activation energies ($\Delta E^{\ddagger}$) reported in the Supporting Information were corrected for zero-point energy (ZPE) from the normal-mode frequency analysis. Electronic energies (ΔE_{DFT}) and entropies (ΔS) were used for the calculations of the standard gas-phase Gibbs free energies (ΔG°_{GP}) at a temperature (T) of 373.15 K.

The solvation free energy contributions for the ideal solution approximation in THF (ΔG_{IS}) and the Gibbs free energies for the two real solution approximations (ΔG_{RS}) were computed with the COSMO-RS method.[63] The respective corrections were calculated using the COSMOthermX version C3.0 program[59] at the recommended BP86 level of theory (for more details, see the Supporting Information). H_2 pressure was set in the calculations to 50 bar, which is the value used in the original experimental study.[47] The chemical composition of the ideal solution (IS) is 0.75 mol KOtBu, 24.6 mol THF, and 0.3 mol dodecane. For the real solution of the solvent-free approximation (***RS-pure***), the starting reaction medium is composed of 0.1 mol KOtBu, 1 mol methyl acetate, and 0.3 mol dodecane. The real solvent model including the THF solvent (***RS-THF***) is made up of 0.75 mol KOtBu, 24.6 mol THF, 1 mol methyl acetate, and 0.3 mol dodecane.

For the microkinetic model, an in-house python script was used and the reaction kinetics were derived for a batch-type reactor (see Section S1 of the Supporting Information). Reaction rate constants were calculated using the Eyring equation. The Gibbs free energy in gas or solvent was computed as outlined in Figure 1 and Section S1 of the Supporting Information. Each solvent model and pathway were examined separately. To compute the kinetic profile of the dynamic reactions, the energy contributions were implemented as a function of alcohol product concentration. Standard conditions in the free energy analysis were defined as the conditions at the start of each catalytic cycle and they were

https://dx.doi.org/10.1021/acs.jpcc.0c09953
J. Phys. Chem. C 2020, 124, 26990−26998

kept unchanged during the microkinetic cycle. Apparent activation energies were calculated in a temperature range of 36 K in five steps (345.5 K, 363.8 K, 373.15 K, 382.5 K, and 392 K). The reaction rates were determined in the initial phase of the reaction. To determine the degree of rate control, the rate constants were varied with factors between 0.996 and 1.004 (0.996, 0.998, 1, 1.002, and 1.004).

3. RESULTS AND DISCUSSION

3.1. Reaction Mechanism. In line with the earlier mechanistic studies,[47,50] here, we considered two competing reaction pathways for ester hydrogenation with the Mn-P,N catalyst depicted in Scheme 1 as the hydrogen shuttle (HS) and the alkoxide (AX) mechanisms.[47,50] Figure 3 presents the

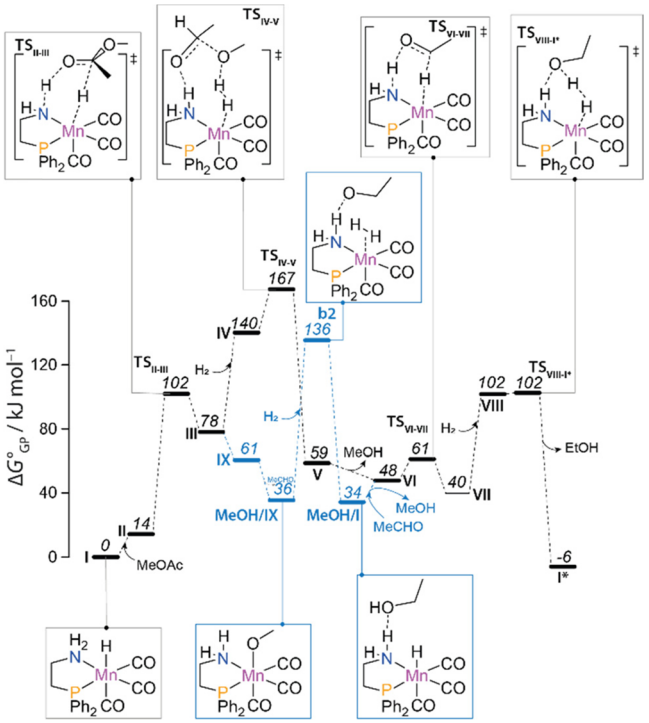

Figure 3. Standard Gibbs free energy diagrams for the HS (black) and AX (gray) pathways at 373 K computed using the *GP* model.

corresponding standard Gibbs free energy diagrams calculated in the *GP* approximation (ΔG°_{GP}). The optimized geometries for all intermediates and transition states with the crucial structural information and the respective ZPE-corrected DFT energies are summarized in Figures S1 and S2. The optimized structures in xyz format are also provided as the Supporting Information.

Both paths start with the coordination of the ester substrate to the Mn−H complex (**I**) forming a weak hydrogen-bonded complex **II**. The subsequent hydride transfer to the carbonyl carbon is the most activated and endergonic step along the reaction path. It proceeds with a standard Gibbs free energy barrier of 102 kJ/mol and results in the intermediate **III**, which is 78 kJ/mol higher in energy than the starting configuration. Next, complex **III** coordinates molecular H_2 to form the σ-complex **IV**. The endergonic nature of this step (**III** + H_2 → **IV**, ΔG°_{GP} = 62 kJ/mol) is due the translational entropy loss and the change of Mn coordination from trigonal pyramidal to an octahedral one upon H_2 complexation. Subsequent heterolytic H_2 dissociation over Mn··· gem-acetal acid−base pair yields state **V** featuring molecular acetaldehyde (AcH), methanol (MeOH), and the catalytic Mn−H species. Next, methanol is released from the reactive ensemble (**V** → **VI**) followed by a hydride transfer to AcH (**VI** → **VII**) that proceeds with a free energy barrier of only 13 kJ/mol. Both steps are exergonic, and they decrease the standard Gibbs free energy of the system by 19 kJ/mol. The catalytic cycle is closed via an endergonic coordination of H_2 to the 5-coordinated Mn-center followed by a barrierless heterolytic H_2 cleavage by which the methoxide moiety is protonated and the initial complex **I** is regenerated.

The alternative AX path diverges from the HS channel after the formation of the gem-acetal intermediate. In this path, the intermediate **III** undergoes a barrierless retro-aldol transformation to form state **IX**. Release of AcH from **IX** produces a Mn−methoxide complex **MeOH/IX** that has previously been proposed as the resting state for the catalytic reaction.[47] Further transformation of this complex requires the replacement of the $^{-}OCH_3$ ligand with a H_2 molecule that is endergonic by 100 kJ/mol. However, as soon as the σ-H_2 complex is formed, it dissociates barrierless to produce **MeOH/I**, which after the MeOH release promotes the reduction of AcH following the HS mechanism.

The direct comparison of these two different pathways and their computed energetics reveals that the HS pathway proceeds through fewer but more endergonic steps, while the AX pathway includes more elementary steps with relatively lower barriers. This suggests that the AX path should in principle be favored. However, the current diagram was constructed using the gas-phase approximation in which the solvation effects were not accounted for. Furthermore, the coordination and decoordination steps were assumed to be elementary within the diagrams. However, a closer look at the computed data reveals that the barrier heights for the elementary steps that do not account for the ligand exchange are comparable. Under the catalytic conditions, the reaction rate will be defined by the whole reaction network and by the composition of the reaction medium.[64] In the next sections, we will separately address the effects of the reactive environment on the reaction energetics and the overall kinetics of the catalytic process.

3.2. Condition-Dependent Free Energy Surfaces. Three distinct solvation models, namely, ***IS***, ***RS-THF***, and ***RS-pure***, introduced in section 2 were considered here. The corresponding results for the HS and AX pathways are summarized in Figure 4a,b, respectively. The in vacuo results obtained with the *GP* model are also presented as a reference with gray dashed lines. In the ideal THF solution (***IS***) model, the solvent-corrected standard free energies (ΔG_{IS}) are obtained by correcting the *GP* results with the estimated free energy of solvation (ΔG_{solv}) of each species in an infinitely diluted pure THF solution. The ***RS*** model accounts for the multicomponent nature of the solution and for the evolution of its composition in the course of the reaction. For the latter, denoted as the gradient correction, the ***RS*** solvent correction terms are computed at varied concentrations of the ester substrate and alcohol products. As a result, the computed energetics become a function of the conversion. The energies of the individual states along the reaction coordinates are presented in the diagram as a range with a color gradient showing the evolution of the reaction medium from low (light color) to high (dark color) conversion levels. We considered

https://dx.doi.org/10.1021/acs.jpcc.0c09953
J. Phys. Chem. C 2020, 124, 26990−26998

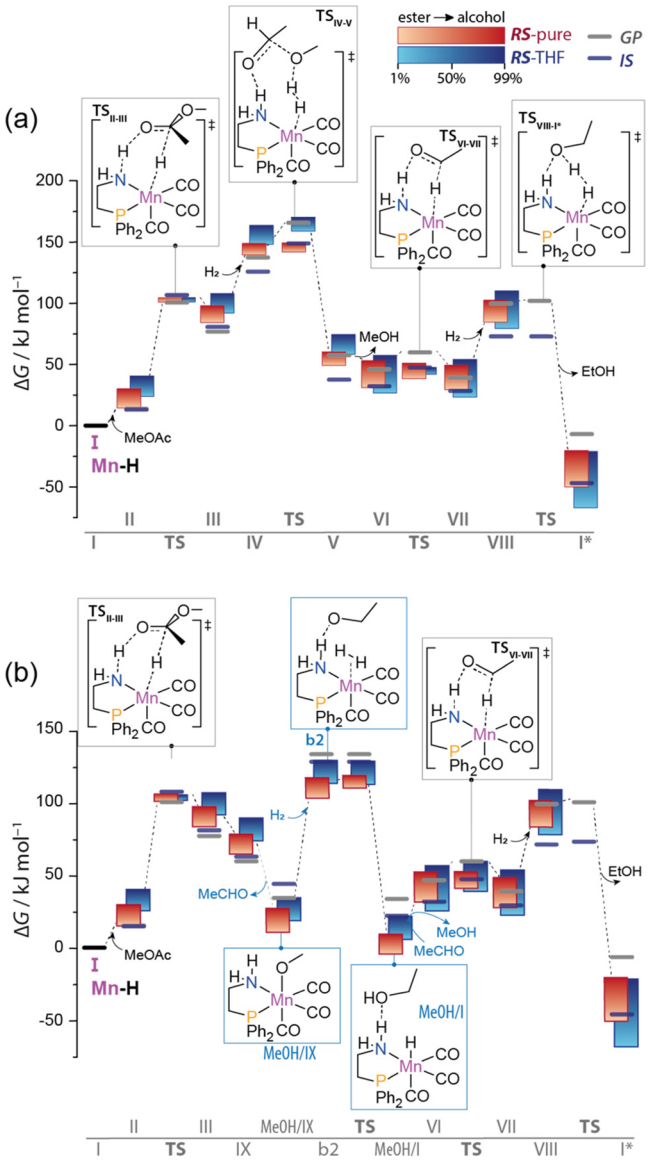

Figure 4. Standard *GP*- and *IS*- as well as condition-dependent *RS*-computed free energy diagrams of the (a) HS and (b) AX reaction pathways. All four methods for calculating the energy contributions are displayed in the diagram.

two situations, namely, when the reaction is carried out in a realistic THF solution (*RS-THF*) and solvent-free in neat ester (*RS-pure*). The medium composition and the reactions conditions do not change within each cycle to maintain the quasi-equilibrium that is required to obey the transition state theory.

The *IS* model shifts the energetics of individual states by $\Delta\Delta G$ ranging from −20 to +20 kJ/mol compared to the levels predicted within the *GP* approximation. The $\Delta\Delta G$ sign indicates relative stabilization (−) and destabilization (+) of the state in solution. The corrections are not uniform along the reaction coordinate. The *IS* correction affects only slightly ($\Delta\Delta G$ = 0 − +7 kJ/mol, Figure 4) the initial steps of ester coordination and activation (steps **I**−**III**). In the AX cycle (Figure 4b), also the subsequent conversion of **III** to **IX** and the formation of the Mn−alkoxide complex (**MeOH**/**IX**) become less favorable within the **IS** model (Figure 4b). However, for the subsequent steps of the catalytic cycle, a pronounced stabilizing effect of the solvent is observed (steps **IV** → **I***, Figure 4a; steps **b2**−**I8**, Figure 4b). The *IS* model consistently stabilizes the respective states by $\Delta\Delta G$ ranging from −25 to −75 kJ/mol. The overall hydrogenation reaction of ester to alcohol (**I** → **I***) is also more exergonic in the *IS* model compared to the *GP* model.

Next, we consider the effect of the dynamic reaction environment during the catalytic process using the gradient *RS* models. The fundamental difference between the *IS* and the *RS* models is that in the latter, the presence of all components of the reaction medium is explicitly taken into account when computing the solvent corrections. This results in a more pronounced destabilization of the initial ester activation steps within the *RS* models. The results of the *RS-THF* model at low conversion levels resemble those obtained with the *IS* pure THF model. However, they deviate strongly for the intermediates with the increasing ester conversion, and accordingly, with the concentration for the alcohol product in the reaction medium. When hydrogenation is carried out using a neat ester substrate (*RS-pure*), the reaction proceeds over a wider range of compositions of the reaction medium. Similar to the *IS* model, the corrections as well as the energy ranges that they cover are not uniform along the reaction coordinates. Both *RS* models predict that the favorability of the overall reaction decreases with the increasing ester conversion.

The *RS-THF* model also predicts notable destabilization of the initial ester coordination steps (**I** → **III**) with $\Delta\Delta G$ = +6 − +31 due to solvation. Unlike the *IS* case considered above, the destabilization effect of *RS-THF* solvation is also observed in the subsequent ester hydrogenolysis steps **III**-**IV** in the HS path ($\Delta\Delta G$ = +1 − +22, Figure 4a), whereas it exerts a pronounced stabilization on the intermediates in the AX path (**MeOH****IX** → **MeOH****I**, $\Delta\Delta G$ = −26 − −1, Figure 4b). The effect of solvation on the subsequent aldehyde reduction (**VI** → **VIII**) varies with the conversion levels. Whereas the respective states are stabilized at low conversion levels, their energies gradually increase as the reaction progresses.

The *RS-pure* model represents the neat catalytic reaction. The reaction environment therefore drastically changes in the course of the reaction from an ester to ethanol solution. Note that the catalytic environment at all conversion levels is modeled as a mixed solvent containing, in addition to the substrate and the product, also 10 mol % KOtBu base promotor. The general trends observed with the *RS-pure* model resemble those established with *RS-THF*, albeit with a more pronounced composition dependency observed at each step. Here, the initial ester coordination (**I** → **III**) is destabilized by $\Delta\Delta G$ = +1 − +19. The destabilizing effect is less pronounced than for the *RS-THF* model. A more pronounced effect of the *RS-pure* model is observed for alkoxide formation and activation, where the species are significantly stabilized (**MeOH****IX** → **MeOH****I**, $\Delta\Delta G$ = −9 − −35, Figure 4b). During aldehyde reduction, the intermediates (**VI** → **VIII**) are, like in the *RS-THF* model, initially stabilized at lower ester conversion levels but destabilize when the ester concentration increases in the mixture ($\Delta\Delta G$ = −19 − +10). The destabilizing effects are pronounced above 90% conversion in intermediates **V** and **VIII** and between 50 and 70% conversion for intermediates **VI** and **VII**. The driving force of the *RS-pure* model is less pronounced than the *RS-THF* model. In the *RS-THF* model, the chemical potential along of the catalytic cycle is changed by $\Delta\Delta G$ = −60 to −16, while for *RS-pure*, the ranges lies between $\Delta\Delta G$ = −44 to −10.

https://dx.doi.org/10.1021/acs.jpcc.0c09953
J. Phys. Chem. C 2020, 124, 26990−26998

3.3. Microkinetic Modeling. In the previous section, we demonstrated a profound impact of the composition of the reaction mixture on the relative stability of intermediates and transition states, and accordingly, on the heights of the free energy barriers and thermodynamics of the elementary steps as well as the overall ester hydrogenation process. In this section, the molecular insights of the different solvation models are converted into macroscopic observable reactivity parameters using a microkinetic model of the dynamic solution (MKM-DS) that explicitly accounts for the dynamic evolution of the reaction phase composition. Concentration dependencies that have been identified in the ***RS*** models are examined to investigate how these effects manifest themselves in the kinetic profiles. The reaction rates for the ***GP***, ***IS***, and ***RS*** models are presented as a function of ester conversion in Figure 5. The ***GP*** model and the ***IS*** model do not account for the changes in the medium composition during the reaction and predict a uniform decrease of the reaction rate with the conversion. The ***IS*** model yields a factor of 10^2−10^3 higher conversion rate via the HS path compared with the ***GP*** model (Figure 5a). This is the direct consequence of the pronounced solvation of the key intermediates and transition states along the catalytic path. The stabilization by the solvent is particularly prominent for the highest energy intermediate, **IV**, and the respective transition state, $\mathbf{TS_{IV\text{-}V}}$, along the HS pathway.

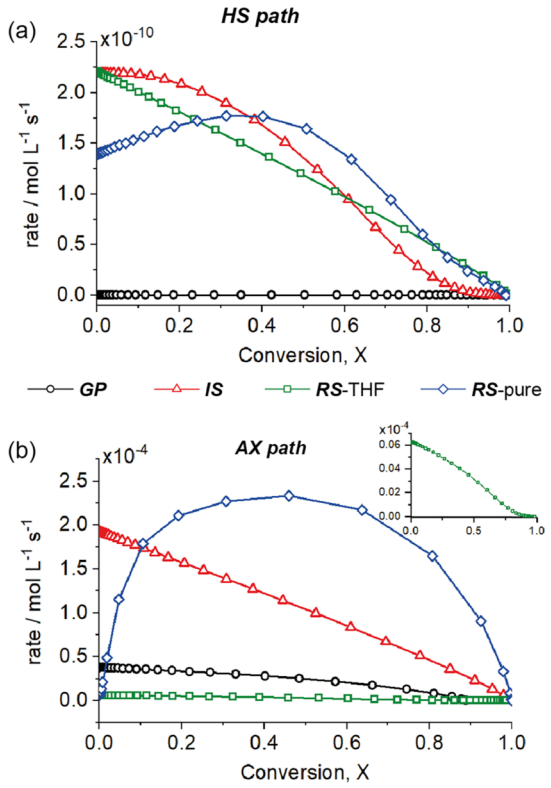

Figure 5. Kinetic profiles of the different solvation models in (a) the HS pathway and (b) the AX pathway. The reaction rate of alcohol production is plotted as a function of conversion.

In the ***RS-THF*** model, at low and intermediate conversions, the rate linearly decreases with substrate depletion. However, at high conversions (X = 0.8−1), the changes in the composition and the polarity of the medium result in substantial deviations from this trend in the AX pathway. The MKM-DS reveals a nonuniform effect of solvation on the relative preference of the two competing reaction paths. Although the ***RS-THF*** model yields a higher rate for the HS pathway than the GP model, for the AX pathway, the ***RS-THF*** rate is five times slower than that in GP (Figure 5b).

The ***RS-pure*** model yields a very different behavior of the reaction rate with conversion than observed in the previous models. In the HS pathway (Figure 5a), the reaction rate starts to increase initially until it peaks at 50% conversion (X = 0.5). Then the rate declines rapidly. The kinetic profile mimics the evolution of the reaction barrier (see Section S4, Supporting Information) for the forward reaction of intermediate **VI** transforming to intermediate **VII**, which decreased rapidly after a conversion level of 50%. The effect observed at higher conversions is in line with that predicted in the ***RS-THF*** model. In the AX pathway (Figure 5b), the ***RS-THF*** model yields a similar shape reaction rate profile. The rate increases until ca. 50% conversion followed by a decline. This behavior is not directly related to the evolution of any particular reaction energy barrier.

The comparison of the kinetic profiles produced by the different solvation models points to a strong and nonlinear effect of the composition of the reaction medium on the catalytic reaction. In line with the formal first-order ester reduction, the idealized ***GP*** and ***IS*** models show a beneficial effect of solvation on the reaction rate that decreases linearly with ester conversion. For all models, the catalytic reaction proceeds predominantly via the AX path with the competitive HS path showing much lower rates. This can also be observed in the microkinetic model when both the AX and HS pathways are combined in a single MKM model. The AX model prevails for each solvent model by more than 99%. The ***RS-THF*** model exhibits minor deviations from the idealized behavior. For the ***RS-pure*** model, the abrupt changes in the solvation environment during the reaction manifest themselves as extreme kinetic effects. The reaction rate instead of uniformely decreasing with conversion passes through a maximum, which can be attributed to swift changes in reaction barriers, especially at low conversions.

Importantly, these drastically different kinetic behaviors do not affect one of the key experimental descriptors for the catalytic reaction, which is the apparent activation energy (E_{act}). Table S1 in the Supporting Information summarizes the MKM-derived E_{act} for the different models and reaction paths at different conversion levels. The changes in the reaction medium composition and the reaction path have a negligible effect on E_{act}. The ***GP*** model yields an E_{act} of 55 kJ/mol, which is considerably smaller than that for the ***IS*** and ***RS*** models (65 and 68 kJ/mol, respectively). The large difference between the ***GP*** and solvation model results point to the importance of the initial ester coordination step for the overall reaction. Despite the less favorable ester activation in the RS models, the high reactivity in this case is probably due to the more efficient promotion of the subsequent steps along the reaction path. It is also important to note that the apparent activation energy does not strictly correspond to the highest energy barrier but is a function of the free energy surface for the overall multistep mechanism. In the next sections, a detailed analysis of the effects of the individual elementary steps on the overall kinetics is presented.

Next, we carried out a degree of rate control analysis to determine the influence of individual reaction steps on the overall reaction for the different models in the AX and HS pathways (Figure 6). The results of this analysis at different

https://dx.doi.org/10.1021/acs.jpcc.0c09953
J. Phys. Chem. C 2020, 124, 26990−26998

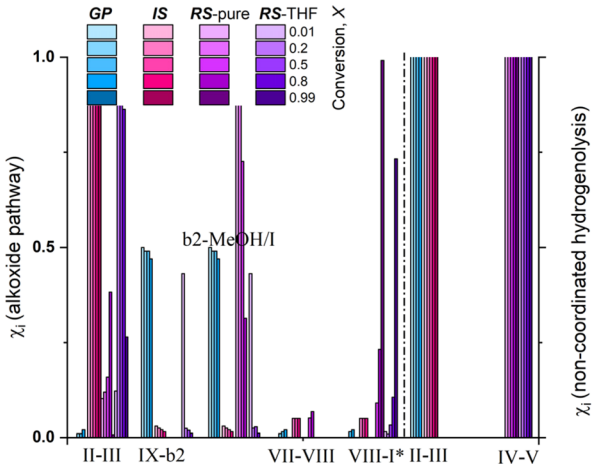

Figure 6. Bar diagram of the degree of rate control in the AX pathway (left) and the pathway proceeding through HS (right). The steps contributing the most are shown for the four different methods at different points of conversions indicated by the color scheme shown at the top.

conversion levels are summarized in Figure 6. For the GP and IS models, in the HS path, the initial ester hydrogenation (**II** → **III**) controls the rate at all conversions. For the RS solvation modes, the initial reduction of the ester by the absorbed hydrogen (**IV** → **V**) is the rate-determining step. A more complex situation is revealed for the AX path, where the alkoxide hydrogenolysis step (**IX** → **MeOH/I**) controls the rate in the GP model, and for the reaction in THF solution (***IS***, ***RS-THF***), the initial ester hydrogenation steps provide the main contribution to the observed rate with a minor contribution of the alkoxide hydrogenolysis (**IX MeOH/I**) and final ethanol production steps of the catalytic cycle (**VII** → **VIII** and **VIII** → **I***). For the pure solution (***RS-pure***), the methanol production step (**b2** → **MeOH/I**) provides the greatest contribution. At higher conversions, the contribution of the latter steps increases for the RS models. This analysis further confirms that the initial ester activation is the key step in the overall reaction with the alkoxide hydrogenolysis additionally contributing to the reaction especially for the idealized ***GP*** and ***IS*** models.

4. CONCLUSIONS

In conclusion, we have investigated the effect of the dynamic evolution of the medium composition on the kinetics of homogeneous ester hydrogenation with the Mn-P,N catalyst. Four different systems were analyzed taking into account different descriptions of the solvent environment and the specific composition of the reaction medium. The effect of the four different models on the reaction energies in different states of solvation was analyzed. In the idealized ***GP*** and ***IS*** models, the energies are stationary, representing the gas-phase corrections and corrections in a pure THF environment, respectively. The operando ***RS-pure*** and ***RS-THF*** models are used to include dynamic corrections and account for the changes of the reaction medium in the course of the reaction. The ***RS-pure*** model serves as an illustration of a reaction medium with reactants, products, additives, and a base present, while the ***RS-THF*** model portrays the reaction medium with THF present. This dynamic model displays kinetics that depend on the change of the Gibbs free energy along the reaction coordinate. In the degree of rate control, the ***GP*** model and the ***RS-pure*** model stand out from the other three models as the recovery of the alkoxide is the rate-controlling step. This coincides with the most energy-demanding step in these models. The apparent activation energies on the other hand have been found to be unaffected by the different corrections because of the assumption that the reaction conditions do not affect substantially the fundamental potential energy surface, while determining the free energy surfaces. From our investigation, we can conclude that while observing strong nonlinear effects in the kinetic models of the dynamic representations, these effects may not manifest themselves within the macroscopic experimentally accessible kinetic descriptors. The RS-type descriptions of the solvent environment that explicitly accounts for the solvent composition are the most representative to practical homogeneous catalyst systems used in the experimental studies.

Thus, our results demonstrate that the model accuracy of the computed parameters of the homogeneous Mn-catalyzed ester hydrogenation reaction depends on the choice of the system description. For predicting the macroscopic average reaction characteristics such as the apparent activation energy, all considered solvent descriptions give a similar outcome. The kinetic behavior of the catalyst systems and their microscopic characteristics, however, depend strongly on the chemical composition of the catalytic system and conditions and should thus best be described with a realistic solvent model allowing for simulating dynamic mixed-solvent environments.

■ ASSOCIATED CONTENT

Supporting Information

The Supporting Information is available free of charge at https://pubs.acs.org/doi/10.1021/acs.jpcc.0c09953.

Optimized structures of reaction intermediates and transition states, apparent activation energies, energy terms from DFT calculation, Gibbs free energies of solvation, activity coefficients of reaction intermediates and transition states for different solvent models, condition dependencies of the reaction free energy barriers, and results of the degree of rate control analysis (PDF)

Optimized structures in xyz format (XYZ)

■ AUTHOR INFORMATION

Corresponding Author

Evgeny A. Pidko − *Inorganic Systems Engineering Group, Department of Chemical Engineering, Delft University of Technology, Delft 2629 HZ, The Netherlands; TheoMAT group, ChemBio Cluster, ITMO University, St. Petersburg 191002, Russia;* orcid.org/0000-0001-9242-9901; Email: e.a.pidko@tudelft.nl

Authors

Annika M. Krieger − *Inorganic Systems Engineering Group, Department of Chemical Engineering, Delft University of Technology, Delft 2629 HZ, The Netherlands;* orcid.org/0000-0002-6178-7041

Pavel Kuliaev − *TheoMAT group, ChemBio Cluster, ITMO University, St. Petersburg 191002, Russia*

Felix Q. Armstrong Hall − *Inorganic Systems Engineering Group, Department of Chemical Engineering, Delft University of Technology, Delft 2629 HZ, The Netherlands*

https://dx.doi.org/10.1021/acs.jpcc.0c09953
J. Phys. Chem. C 2020, 124, 26990−26998

Dapeng Sun − *Inorganic Systems Engineering Group, Department of Chemical Engineering, Delft University of Technology, Delft 2629 HZ, The Netherlands*

Complete contact information is available at: https://pubs.acs.org/10.1021/acs.jpcc.0c09953

Notes

The authors declare no competing financial interest.
Source data for the manuscript and the supporting information are provided at https://doi.org/10.4121/13214171.

■ ACKNOWLEDGMENTS

Authors acknowledge financial support from the European Research Council (ERC) under the European Union's Horizon 2020 research and innovation programme (grant agreement No. 725686). The authors thank the Netherlands Organization for Scientific Research (NWO) for the access to SURFsara computational facilities.

■ REFERENCES

(1) Schober, L. Sustainable Synthesis of Pharmaceuticals: Using Transition-Metal Complexes as Catalysts. *Green Process. Synth.* **2018**, *7*, 558−559.
(2) Gunanathan, C.; Milstein, D. Applications of Acceptorless Dehydrogenation and Related Transformations in Chemical Synthesis. *Science* **2013**, *341*, 1229712−1229712.
(3) Irrgang, T.; Kempe, R. 3d-Metal Catalyzed N- and C-Alkylation Reactions via Borrowing Hydrogen or Hydrogen Autotransfer. *Chem. Rev.* **2019**, *119*, 2524−2549.
(4) Alig, L.; Fritz, M.; Schneider, S. First-Row Transition Metal (De)Hydrogenation Catalysis Based On Functional Pincer Ligands. *Chem. Rev.* **2019**, *119*, 2681−2751.
(5) Liu, W.; Sahoo, B.; Junge, K.; Beller, M. Cobalt Complexes as an Emerging Class of Catalysts for Homogeneous Hydrogenations. *Acc. Chem. Res.* **2018**, *51*, 1858−1869.
(6) Wei, D.; Darcel, C. Iron Catalysis in Reduction and Hydrometalation Reactions. *Chem. Rev.* **2019**, *119*, 2550−2610.
(7) Formenti, D.; Ferretti, F.; Scharnagl, F. K.; Beller, M. Reduction of Nitro Compounds Using 3d-Non-Noble Metal Catalysts. *Chem. Rev.* **2019**, *119*, 2611−2680.
(8) Reid, J. P.; Sigman, M. S. Comparing Quantitative Prediction Methods for the Discovery of Small-Molecule Chiral Catalysts. *Nat. Rev. Chem.* **2018**, *2*, 290−305.
(9) Quesne, M. G.; Silveri, F.; de Leeuw, N. H.; Catlow, C. R. A. Advances in Sustainable Catalysis: A Computational Perspective. *Front. Chem.* **2019**, *7*, 182.
(10) Nandy, A.; Zhu, J.; Janet, J. P.; Duan, C.; Getman, R. B.; Kulik, H. J. Machine Learning Accelerates the Discovery of Design Rules and Exceptions in Stable Metal−Oxo Intermediate Formation. *ACS Catal.* **2019**, *9*, 8243−8255.
(11) Kulik, H. J. Making Machine Learning a Useful Tool in the Accelerated Discovery of Transition Metal Complexes. *WIREs Comput. Mol. Sci.* **2020**, *10*, e1439.
(12) Santiago, C. B.; Guo, J.-Y.; Sigman, M. S. Predictive and Mechanistic Multivariate Linear Regression Models for Reaction Development. *Chem. Sci.* **2018**, *9*, 2398−2412.
(13) Vogiatzis, K. D.; Polynski, M. V.; Kirkland, J. K.; Townsend, J.; Hashemi, A.; Liu, C.; Pidko, E. A. Computational Approach to Molecular Catalysis by 3d Transition Metals: Challenges and Opportunities. *Chem. Rev.* **2019**, *119*, 2453−2523.
(14) Klippenstein, S. J.; Pande, V. S.; Truhlar, D. G. Chemical Kinetics and Mechanisms of Complex Systems: A Perspective on Recent Theoretical Advances. *J. Am. Chem. Soc.* **2014**, *136*, 528−546.
(15) Cohen, A. J.; Mori-Sánchez, P.; Yang, W. Challenges for Density Functional Theory. *Chem. Rev.* **2012**, *112*, 289−320.
(16) Qi, S.-C.; Hayashi, J.; Zhang, L. Recent Application of Calculations of Metal Complexes Based on Density Functional Theory. *RSC Adv.* **2016**, *6*, 77375−77395.
(17) Brémond, E.; Ciofini, I.; Sancho-García, J. C.; Adamo, C. Nonempirical Double-Hybrid Functionals: An Effective Tool for Chemists. *Acc. Chem. Res.* **2016**, *49*, 1503−1513.
(18) Maier, T. M.; Arbuznikov, A. V.; Kaupp, M. Local Hybrid Functionals: Theory, Implementation, and Performance of an Emerging New Tool in Quantum Chemistry and Beyond. *WIREs Comput. Mol. Sci.* **2019**, *9*, e1378.
(19) Ghosh, S.; Verma, P.; Cramer, C. J.; Gagliardi, L.; Truhlar, D. G. Combining Wave Function Methods with Density Functional Theory for Excited States. *Chem. Rev.* **2018**, *118*, 7249−7292.
(20) Pidko, E. A. Toward the Balance between the Reductionist and Systems Approaches in Computational Catalysis: Model versus Method Accuracy for the Description of Catalytic Systems. *ACS Catal.* **2017**, *7*, 4230−4234.
(21) Mennucci, B., Cammi, R., Eds.; *Continuum Solvation Models in Chemical Physics*; John Wiley & Sons, Ltd: Chichester, UK, 2007. DOI: 10.1002/9780470515235.
(22) Cramer, C. J.; Truhlar, D. G. Implicit Solvation Models: Equilibria, Structure, Spectra, and Dynamics. *Chem. Rev.* **1999**, *99*, 2161−2200.
(23) Cramer, C. J.; Truhlar, D. G. A Universal Approach to Solvation Modeling. *Acc. Chem. Res.* **2008**, *41*, 760−768.
(24) Grajciar, L.; Heard, C. J.; Bondarenko, A. A.; Polynski, M. V.; Meeprasert, J.; Pidko, E. A.; Nachtigall, P. Towards Operando Computational Modeling in Heterogeneous Catalysis. *Chem. Soc. Rev.* **2018**, *47*, 8307−8348.
(25) Kuliaev, P. O.; Pidko, E. A. Operando Modeling of Multicomponent Reactive Solutions in Homogeneous Catalysis: From Non-standard Free Energies to Reaction Network Control. *ChemCatChem* **2020**, *12*, 795−802.
(26) Kim, Y.; Mohrig, J. R.; Truhlar, D. G. Free-Energy Surfaces for Liquid-Phase Reactions and Their Use To Study the Border Between Concerted and Nonconcerted α,β-Elimination Reactions of Esters and Thioesters. *J. Am. Chem. Soc.* **2010**, *132*, 11071−11082.
(27) Werkmeister, S.; Junge, K.; Beller, M. Catalytic Hydrogenation of Carboxylic Acid Esters, Amides, and Nitriles with Homogeneous Catalysts. *Org. Process Res. Dev.* **2014**, *18*, 289−302.
(28) Pritchard, J.; Filonenko, G. A.; van Putten, R.; Hensen, E. J. M.; Pidko, E. A. Heterogeneous and Homogeneous Catalysis for the Hydrogenation of Carboxylic Acid Derivatives: History, Advances and Future Directions. *Chem. Soc. Rev.* **2015**, *44*, 3808−3833.
(29) Dub, P. A.; Batrice, R. J.; Gordon, J. C.; Scott, B. L.; Minko, Y.; Schmidt, J. G.; Williams, R. F. Engineering Catalysts for Selective Ester Hydrogenation. *Org. Process Res. Dev.* **2020**, *24*, 415−442.
(30) Dub, P. A.; Ikariya, T. Catalytic Reductive Transformations of Carboxylic and Carbonic Acid Derivatives Using Molecular Hydrogen. *ACS Catal.* **2012**, *2*, 1718−1741.
(31) Kuriyama, W.; Matsumoto, T.; Ogata, O.; Ino, Y.; Aoki, K.; Tanaka, S.; Ishida, K.; Kobayashi, T.; Sayo, N.; Saito, T. Catalytic Hydrogenation of Esters. Development of an Efficient Catalyst and Processes for Synthesising (R)-1,2-Propanediol and 2-(l-Menthoxy)-Ethanol. *Org. Process Res. Dev.* **2012**, *16*, 166−171.
(32) Spasyuk, D.; Smith, S.; Gusev, D. G. Replacing Phosphorus with Sulfur for the Efficient Hydrogenation of Esters. *Angew. Chem. Int. Ed.* **2013**, *125*, 2598−2602.
(33) Filonenko, G. A.; Aguila, M. J. B.; Schulpen, E. N.; Van Putten, R.; Wiecko, J.; Müller, C.; Lefort, L.; Hensen, E. J. M.; Pidko, E. A. Bis-N-Heterocyclic Carbene Aminopincer Ligands Enable High Activity in Ru-Catalyzed Ester Hydrogenation. *J. Am. Chem. Soc.* **2015**, *137*, 7620−7623.
(34) Zell, T.; Ben-David, Y.; Milstein, D. Unprecedented Iron-Catalyzed Ester Hydrogenation. Mild, Selective, and Efficient Hydrogenation of Trifluoroacetic Esters to Alcohols Catalyzed by an Iron Pincer Complex. *Angew. Chem., Int. Ed.* **2014**, *126*, 4773−4777.

(35) Werkmeister, S.; Junge, K.; Wendt, B.; Alberico, E.; Jiao, H.; Baumann, W.; Junge, H.; Gallou, F.; Beller, M. Hydrogenation of Esters to Alcohols with a Well-Defined Iron Complex. *Angew. Chem., Int. Ed.* **2014**, *53*, 8722−8726.
(36) Chakraborty, S.; Dai, H.; Bhattacharya, P.; Fairweather, N. T.; Gibson, M. S.; Krause, J. A.; Guan, H. Iron-Based Catalysts for the Hydrogenation of Esters to Alcohols. *J. Am. Chem. Soc.* **2014**, *136*, 7869−7872.
(37) Spasyuk, D.; Smith, S.; Gusev, D. G. From Esters to Alcohols and Back with Ruthenium and Osmium Catalysts. *Angew. Chem., Int. Ed.* **2012**, *124*, 2826−2829.
(38) Mukherjee, A.; Nerush, A.; Leitus, G.; Shimon, L. J. W.; Ben David, Y.; Espinosa Jalapa, N. A.; Milstein, D. Manganese-Catalyzed Environmentally Benign Dehydrogenative Coupling of Alcohols and Amines to Form Aldimines and H 2 : A Catalytic and Mechanistic Study. *J. Am. Chem. Soc.* **2016**, *138*, 4298−4301.
(39) Mastalir, M.; Glatz, M.; Gorgas, N.; Stöger, B.; Pittenauer, E.; Allmaier, G.; Veiros, L. F.; Kirchner, K. Divergent Coupling of Alcohols and Amines Catalyzed by Isoelectronic Hydride Mn I and Fe II PNP Pincer Complexes. *Chem. Eur. J.* **2016**, *22*, 12316−12320.
(40) Elangovan, S.; Garbe, M.; Jiao, H.; Spannenberg, A.; Junge, K.; Beller, M. Hydrogenation of Esters to Alcohols Catalyzed by Defined Manganese Pincer Complexes. *Angew. Chem., Int. Ed.* **2016**, *128*, 15590−15594.
(41) Zirakzadeh, A.; Kirchner, K.; Roller, A.; Stöger, B.; Carvalho, M. D.; Ferreira, L. P. Synthesis, Coordination Behavior and Structural Features of Chiral Iron(II) PNP Diferrocene Complexes. *RSC Adv.* **2016**, *6*, 11840−11847.
(42) Spasyuk, D.; Smith, S.; Gusev, D. G. From Esters to Alcohols and Back with Ruthenium and Osmium Catalysts. *Angew. Chem., Int. Ed.* **2012**, *51*, 2772−2775.
(43) Gusev, D. G. Dehydrogenative Coupling of Ethanol and Ester Hydrogenation Catalyzed by Pincer-Type YNP Complexes. *ACS Catal.* **2016**, *6*, 6967−6981.
(44) Kim, D.; Le, L.; Drance, M. J.; Jensen, K. H.; Bogdanovski, K.; Cervarich, T. N.; Barnard, M. G.; Pudalov, N. J.; Knapp, S. M. M.; Chianese, A. R. Ester Hydrogenation Catalyzed by CNN-Pincer Complexes of Ruthenium. *Organometallics* **2016**, *35*, 982−989.
(45) Elangovan, S.; Garbe, M.; Jiao, H.; Spannenberg, A.; Junge, K.; Beller, M. Hydrogenation of Esters to Alcohols Catalyzed by Defined Manganese Pincer Complexes. *Angew. Chem., Int. Ed.* **2016**, *55*, 15364−15368.
(46) Filonenko, G. A.; van Putten, R.; Hensen, E. J. M.; Pidko, E. A. Catalytic (de)Hydrogenation Promoted by Non-Precious Metals − Co, Fe and Mn: Recent Advances in an Emerging Field. *Chem. Soc. Rev.* **2018**, *47*, 1459−1483.
(47) van Putten, R.; Uslamin, E. A.; Garbe, M.; Liu, C.; Gonzalez-de-Castro, A.; Lutz, M.; Junge, K.; Hensen, E. J. M.; Beller, M.; Lefort, L.; et al. Non-Pincer-Type Manganese Complexes as Efficient Catalysts for the Hydrogenation of Esters. *Angew. Chem., Int. Ed.* **2017**, *56*, 7531−7534.
(48) Nguyen, D. H.; Trivelli, X.; Capet, F.; Paul, J.-F.; Dumeignil, F.; Gauvin, R. M. Manganese Pincer Complexes for the Base-Free, Acceptorless Dehydrogenative Coupling of Alcohols to Esters: Development, Scope, and Understanding. *ACS Catal.* **2017**, *7*, 2022−2032.
(49) Widegren, M. B.; Harkness, G. J.; Slawin, A. M. Z.; Cordes, D. B.; Clarke, M. L. A Highly Active Manganese Catalyst for Enantioselective Ketone and Ester Hydrogenation. *Angew. Chem., Int. Ed.* **2017**, *56*, 5825−5828.
(50) Liu, C.; van Putten, R.; Kulyaev, P. O.; Filonenko, G. A.; Pidko, E. A. Computational Insights into the Catalytic Role of the Base Promoters in Ester Hydrogenation with Homogeneous Non-Pincer-Based Mn-P,N Catalyst. *J. Catal.* **2018**, *363*, 136−143.
(51) Chowdhury, A.; Biswas, S.; Pramanik, A.; Sarkar, P. Mechanistic Insights into the Non-Bifunctional Hydrogenation of Esters by Co(II) Pincer Complexes: A DFT Study. *Dalton Trans.* **2019**, *48*, 16083−16090.
(52) Mandal, S. C.; Rawat, K. S.; Nandi, S.; Pathak, B. Theoretical Insights into CO 2 Hydrogenation to Methanol by a Mn−PNP Complex. *Catal. Sci. Technol.* **2019**, *9*, 1867−1878.
(53) Dub, P. A.; Gordon, J. C. The Role of the Metal-Bound N−H Functionality in Noyori-Type Molecular Catalysts. *Nat. Rev. Chem.* **2018**, *2*, 396−408.
(54) Dub, P. A.; Henson, N. J.; Martin, R. L.; Gordon, J. C. Unravelling the Mechanism of the Asymmetric Hydrogenation of Acetophenone by [RuX_2(Diphosphine)(1,2-Diamine)] Catalysts. *J. Am. Chem. Soc.* **2014**, *136*, 3505−3521.
(55) Wohlfarth, C.. *Dielectric Constant of Methyl Acetate*; Lechner, M. D., Ed.; Springer-Verlag Berlin Heidelberg, 2008; 171−171. DOI: 10.1007/978-3-540-75506-7_75.
(56) *Methanol Dielectric Constant: Datasheet from "Dortmund Data Bank (DDB) -- Thermophysical Properties Edition 2014" in SpringerMaterials* (https://Materials.Springer.Com/Thermophysical/Docs/Dec_c110). Springer-Verlag Berlin Heidelberg & DDBST GmbH, Oldenburg, Germany.
(57) *Ethanol Dielectric Constant: Datasheet from "Dortmund Data Bank (DDB) -- Thermophysical Properties Edition 2014" in SpringerMaterials* (Https://Materials.Springer.Com/Thermophysical/Docs/Dec_c11). Springer-Verlag Berlin Heidelberg & DDBST GmbH, Oldenburg, Germany.
(58) Ochterski, J. W. *Thermochemistry in Gaussian*. Gaussian, Inc. 2000, 1−19.
(59) Klamt, A. Conductor-like Screening Model for Real Solvents: A New Approach to the Quantitative Calculation of Solvation Phenomena. *J. Phys. Chem.* **1995**, *99*, 2224−2235.
(60) Frisch, M. J.; Trucks, G. W.; Schlegel, H. B.; Scuseria, G. E.; Robb, M. A.; Cheeseman, J. R.; Scalmani, G.; Barone, V.; Petersson, G. A.; Nakatsuji, H.; et al. *Gaussian16 Revision C.01*. 2016.
(61) Adamo, C.; Barone, V. Toward Reliable Density Functional Methods without Adjustable Parameters: The PBE0 Model. *J. Chem. Phys.* **1999**, *110*, 6158−6170.
(62) Grimme, S.; Ehrlich, S.; Goerigk, L. Effect of the Damping Function in Dispersion Corrected Density Functional Theory. *J. Comput. Chem.* **2011**, *32*, 1456−1465.
(63) Klamt, A. The COSMO and COSMO-RS Solvation Models. *WIREs Comput. Mol. Sci.* **2011**, *1*, 699−709.
(64) Temkin, O. N.. Effect of Medium on Reaction Rates in Homogeneous Catalysis with Metal Complexes. In *Homogeneous Catalysis with Metal Complexes*; John Wiley & Sons, Ltd: Chichester, UK, 2012; 741−796. DOI: 10.1002/9781119966227.ch8.

https://dx.doi.org/10.1021/acs.jpcc.0c09953
J. Phys. Chem. C 2020, 124, 26990−26998